

2D MATERIALS

Imaging quantum melting in a disordered 2D Wigner solid

Ziyu Xiang^{1,2,3,†}, Hongyuan Li^{1,2,3,†}, Jianghan Xiao^{1,2,3,†}, Mit H. Naik^{1,3}, Zhehao Ge¹, Zehao He¹, Sudi Chen^{1,3,4}, Jiahui Nie¹, Shiyu Li¹, Yifan Jiang¹, Renee Sailus⁵, Rounak Banerjee⁵, Takashi Taniguchi⁶, Kenji Watanabe⁷, Sefaattin Tongay⁵, Steven G. Louie^{1,3}, Michael F. Crommie^{1,3,4*}, Feng Wang^{1,3,4*}

Two-dimensional strongly interacting electrons crystallize into a solid phase known as the Wigner crystal at low densities and form a Fermi liquid at high densities. At intermediate densities, the two-dimensional solid evolves into a strongly correlated liquid phase around a critical density. We observed this quantum melting of a disordered Wigner solid in bilayer molybdenum diselenide (MoSe₂) using a noninvasive scanning tunneling microscopy imaging technique. At low densities, the Wigner solid forms nanocrystalline domains pinned by local disorder. It exhibits a quantum densification behavior with increased densities in the solid phase. Above a threshold density, the Wigner solid melts locally and enters a mixed phase in which solid and liquid regions coexist. The liquid regions expand and form a percolation network at even higher densities.

Understanding strongly correlated electron phenomena arising from the interplay between Coulomb energy and electron kinetic energy is a central topic in condensed matter physics (1–9). The two-dimensional electron gas (2DEG) at very high densities is well described by a weakly interacting Fermi liquid theory (10), whereas in the low-density limit, electrons solidify into a Wigner crystal in which Coulomb energy dominates over kinetic energy (1, 11, 12). At intermediate densities, however, the competition between Coulomb energy and kinetic energy is more pronounced and drives the emergence of exotic strongly correlated phases (12, 13). Great experimental and theoretical effort has been made to understand the quantum melting of Wigner crystals and the resulting correlated electron phenomena at intermediate electron densities (13–22). Notable non-Fermi liquid transport behavior, including an insulator-to-metal transition and anomalous temperature-dependent and magnetic field-dependent resistivity, have been observed experimentally in various 2DEG systems (8, 13, 21–26). Although different theoretical pictures have been proposed to describe the experimental data (14–20, 27), no consensus on the proper description of Wigner crystal quantum melting and resulting correlated electron states at intermediate electron densities has been reached. For substantial further understanding of the microscopic nature of Wigner solid quantum melting, experimental measurements capable of probing correlated electronic structure at both atomic and mesoscopic scales are necessary.

Here, we describe the use of a noninvasive imaging technique to visualize a Wigner solid of holes, including its densification and quantum melting, in bilayer molybdenum diselenide (biMoSe₂). At low hole

density, we observed a disordered Wigner solid that exhibits a local triangular lattice but no long-range crystalline order owing to point defects that pin the Wigner solid and induce nanocrystalline domains. The Wigner solid exhibits an unusual densification behavior as the hole density is increased: Instead of a continuous contraction of the lattice constant as expected for a perfect Wigner crystal, the holes appear to evolve by means of a quantum superposition state. Above a critical hole density of $n_c = 5.7 \times 10^{12} \text{ cm}^{-2}$, the Wigner solid starts to melt and enters a mixed phase, with coexisting solid and liquid regions.

Noninvasive STM imaging in biMoSe₂

The ratio between Coulomb energy and kinetic energy in a 2DEG is characterized by a single dimensionless parameter $r_s = \frac{a_0}{a_B} = \frac{m^* e^2}{4\pi\epsilon\hbar^2\sqrt{\pi n}}$ where a_0 is the average interparticle distance, a_B is the effective Bohr radius, n is the electron/hole density, ϵ is the effective dielectric constant, and m^* is the electron effective mass. Quantum Monte Carlo simulations suggest that 2D Wigner crystals melt into a liquid phase for $r_s^* \approx 38$ (12, 14, 28). Atomically thin 2D materials provide a rich platform to explore Wigner crystal physics. Previously, generalized Wigner crystals stabilized by a moiré superlattice have been imaged in tungsten diselenide (WSe₂)/tungsten disulfide (WS₂) heterostructures (6), and more recently, magnetic field-stabilized Wigner crystals have been imaged in graphene samples (9). Optical spectroscopy, on the other hand, has suggested that “bare” Wigner crystals (without assistance from a moiré superlattice or magnetic field) can exist in transition-metal dichalcogenide (TMD) layers (29, 30). We chose the 2D hole gas (2DHG) in biMoSe₂ as a model system to image bare Wigner solid and its quantum melting behavior because of the large hole effective mass $m^* \approx 1.26m_e$ predicted by our ab initio calculation [(31), section 3], which helps to increase r_s . Increased r_s facilitates the formation of Wigner solids over a large hole density range and helps them to be more robust against temperature fluctuation and weak disorder. The experimental setup used to incorporate biMoSe₂ into a van der Waals heterostructure device stack is illustrated in Fig. 1A. We tuned the hole density in biMoSe₂ by applying a bottom gate voltage (V_{BG}) between a graphite bottom gate (BG) and the biMoSe₂. A graphene nanoribbon (GNR) array was specially prepared as the electrical contact to biMoSe₂, thus reducing contact resistance and facilitating effective gating. An optical micrograph of the biMoSe₂ heterostructure device is shown in Fig. 1B, with biMoSe₂, GNR, and BG regions indicated with green, blue, and red dashed lines, respectively.

We used a noninvasive valence band edge (VBE) tunnel current measurement technique (32) that enables the probing of Wigner solids in hole-doped biMoSe₂ with minimal tip perturbation. The schematic in Fig. 1C outlines the basic principle of the measurement by showing the band alignment between the tip of scanning tunneling microscopy (STM) and hole-doped biMoSe₂. Because of the non-negligible work function difference between the STM tip (made of platinum/iridium) and biMoSe₂, the tip perturbation cannot be neglected in most cases and often has a fatal impact on fragile correlated electrons. To overcome this issue, we tuned the sample-tip bias voltage (V_{bias}) so that the vacuum energy levels of both the tip and biMoSe₂ were aligned, thus canceling the work function difference. This minimizes the local electric field near the tip apex and ensures that the integrity of the Wigner solid is maintained [(31), section 1]. The alignment of the TMD and tip vacuum levels can be achieved by moving the tip chemical potential within the biMoSe₂ bandgap. In this case, the tunnel current arises exclusively from doped holes at the biMoSe₂ VBE without impact from higher-energy states. The VBE tunnel current directly reflects the spatial distribution of doped holes similar to previous demonstrations of VBE current mapping of Wigner molecules (32).

The tunnel current (I - V) characteristic on a log scale is shown in Fig. 1D as a function of V_{BG} for hole-doped biMoSe₂, with a relatively large tip-sample separation [determined by the setpoint condition $V_{bias} = -3 \text{ V}$, setpoint current (I_{sp}) = 20 pA, tip lift height (h_{tip}) = -30 pm,

¹Department of Physics, University of California at Berkeley, Berkeley, CA, USA. ²Graduate Group in Applied Science and Technology, University of California at Berkeley, Berkeley, CA, USA. ³Materials Sciences Division, Lawrence Berkeley National Laboratory, Berkeley, CA, USA. ⁴Kavli Energy Nano Sciences Institute, University of California Berkeley and the Lawrence Berkeley National Laboratory, Berkeley, CA, USA. ⁵School for Engineering of Matter, Transport and Energy, Arizona State University, Tempe, AZ, USA. ⁶International Center for Materials Nanoarchitectonics, National Institute for Materials Science, Tsukuba, Japan. ⁷Research Center for Functional Materials, National Institute for Materials Science, Tsukuba, Japan. *Corresponding author. Email: crommie@berkeley.edu (M.F.C.); fengwang76@berkeley.edu (F.W.) †These authors contributed equally to this work.

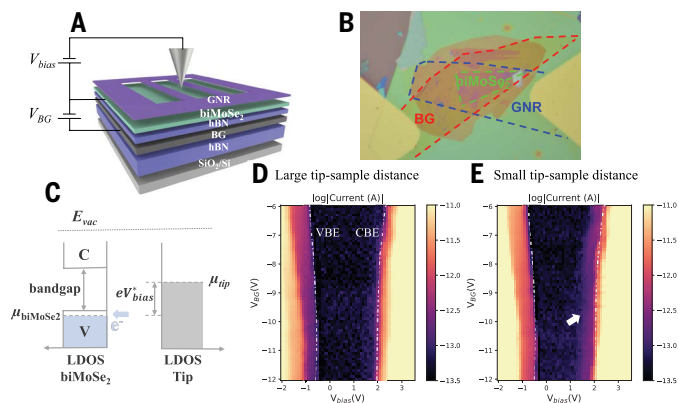


Fig. 1. Noninvasive VBE tunnel current measurement of biMoSe₂. (A) A schematic of the STM measurement setup for gate-tunable biMoSe₂. The biMoSe₂ is placed on top of a 50-nm-thick hexagonal boron nitride (hBN) layer and a graphite substrate that defines the back gate (BG). A back gate voltage V_{BG} is applied to control the charge carrier density in the biMoSe₂. A bias voltage V_{bias} is applied to the biMoSe₂ relative to the STM tip to induce tunnel current. A graphene nanoribbon (GNR) array is placed on top of the biMoSe₂ as a contact electrode. (B) Optical microscope image of the device heterostructure. The biMoSe₂, GNR, and BG are outlined in green, blue, and red, respectively. (C) Schematic energy diagram for the valence band edge (VBE) tunnel current measurement of hole-doped biMoSe₂. The biMoSe₂ chemical potential, μ_{biMoSe_2} , is near the valence band edge. When μ_{tip} is aligned within the bandgap of biMoSe₂, the tunnel current arises from doped holes at the VBE. V_{bias} is tuned to roughly align the vacuum energy levels of the tip and biMoSe₂ so that the electric field near the tip apex is minimized. The gap between μ_{tip} and μ_{biMoSe_2} is denoted V_{bias}^* instead of V_{bias} because the real bias on the tunneling junction V_{bias}^* is reduced by the large contact resistance (the Schottky barrier). (D) The tunnel current I - V characteristics as a function of V_{BG} for hole-doped biMoSe₂ with a large tip-sample distance. The current is plotted on an absolute log scale. The VBE and CBE are indicated with white dashed curves. (E) The tunnel current I - V characteristics as a function of V_{BG} for hole-doped biMoSe₂ with a small tip-sample distance, similar to that in (D). The white arrow indicates the VBE tunnel current. $T = 5.4$ K for all the above measurements.

and temperature ($T = 5.4$ K) (31). Negligible tunnel current occurs for $-0.5\text{ V} < V_{bias} < 2$ V, which corresponds to the biMoSe₂ semiconducting band gap [the VBE and conduction band edge (CBE) are indicated in Fig. 1D with dot-dashed lines]. The bandgap shows an apparent increase as V_{BG} is increased. This is likely because the contact resistance between the biMoSe₂ and GNR contacts increases at lower hole doping, causing part of the bias voltage to drop at the contact rather than at the tip-sample gap. At large tip-sample separation, the VBE tunnel current is lower than the measurement noise floor in the bandgap region and is not observable. When the tip-sample distance is reduced (setpoint condition: $V_{bias} = -3$ V, $I_{sp} = 20$ pA, $h_{tip} = -90$ pm), however, VBE tunnel current starts to appear in the band gap (Fig. 1E, white arrow).

Visualizing the hole Wigner solid

Spatially mapping the VBE tunnel current allows us to visualize the Wigner solid within biMoSe₂. The VBE tunnel current map obtained at a hole density of $n = 5.3 \times 10^{12} \text{ cm}^{-2}$ is shown in Fig. 2A [with $V_{BG} = -8$ V, $V_{bias} = 1.9$ V to minimize tip perturbation; details on determining V_{bias} with minimized tip perturbation are available in (31), section 1]. Each bright dot in Fig. 2A indicates a localized hole in biMoSe₂. The corresponding STM topographic image by using conventional constant current mode is shown in Fig. 2B ($V_{bias} = -3$ V, $I_{sp} = 20$ pA). The bright defects in Fig. 2B correspond to charged defects, which act as local pinning centers in the Wigner solid of Fig. 2A (Fig. 2B also contains weaker features arising from isovalent defects) [(31), section 1] (33–35). The Wigner solid exhibits a nanocrystalline phase with

different nanocrystalline domains but no long-range crystalline order owing to defect-induced disorder. The fast Fourier transform (FFT) patterns in Fig. 2, D to F, correspond to regions (i), (ii), and (iii), respectively, in Fig. 2A. Each shows a local hexagonal lattice with six distinct diffraction spots (Fig. 2, D to F, solid red dots), but the lattice orientation is random in different regions. The orientational coherence of the Wigner solid is disrupted by disorder in the biMoSe₂ semiconductor.

We used the Delaunay triangulation and Voronoi cell partition method to systematically analyze the disordered Wigner solid. This methodology is useful for quantitatively analyzing the lattice structure of disordered crystals [it has been used, for example, to analyze vortex lattice in layered superconductors (36, 37)]. We show in Fig. 2C the Voronoi cell diagram for the disordered Wigner solid shown in Fig. 2A [(31), section 2]. Each vertex corresponds to a single hole, and each edge connects nearest-neighbor holes. In an ideal Wigner crystal, each hole would have six nearest neighbors, whereas in our disordered Wigner solid, a substantial number of dislocations can be seen (a dislocation is a five-membered ring of nearest neighbors adjacent to a seven-membered ring). We counted 43 dislocations out of the 237 holes shown in Fig. 2C. We have color-coded in Fig. 2C the Voronoi cell: Blue dashed lines connect the vertices of dislocations, and solid lines connect to holes without dislocations. The three different colors of the solid lines in Fig. 2C (light blue, light orange, and dark red) trace the lattice orientation of the crystalline domains. Dislocations frequently appear in pairs or defect lines that separate regions without dislocations into randomly oriented nanocrystalline domains.

We studied the evolution of the disordered Wigner solid as a function of hole density by varying the gate voltage V_{BG} . In Fig. 2, A and G to I, we show the VBE tunnel current maps for biMoSe₂ as the hole density is increased from 4.2×10^{12} to $7.0 \times 10^{12} \text{ cm}^{-2}$ [discussion of choosing a noninvasive V_{bias} is available in (31), section 1]. For low charge density ($V_{BG} \geq -8$ V), the holes remain well separated and form a solid phase. As V_{BG} is reduced, however, the Wigner solid becomes denser, and the spatial extent (full width at half maximum) of each hole wave function shrinks. As V_{BG} is reduced beyond the threshold of $V_{BG} = -8$ V, regions of the Wigner solid become “blurred” and no longer exhibit well-separated holes. This behavior indicates the onset of local melting of the Wigner solid. Further reduction of V_{BG} causes the melted regions to expand and eventually form a percolation network at very high hole density ($n \approx 7.0 \times 10^{12} \text{ cm}^{-2}$).

Quantum densification

The mechanism by which the density of holes increases with decreased V_{BG} for our disordered Wigner solid is different from the smooth lattice constant variation expected for an ideal Wigner crystal. We observed instead a highly local process that we call “quantum densification.” In this process, individual holes are added quantum mechanically into local regions constrained by disorders, and partially delocalized hole wave functions are observed during the transition between two well-defined solid lattice configurations.

The quantum densification process can be seen in Fig. 3, which shows a small region of the Wigner solid imaged under conditions in which the hole density is gradually increased through a combination of increased V_{bias} and decreased V_{BG} as shown in Fig. 3, A to F (increasing V_{bias} has the same effect locally as decreasing V_{BG}). In these conditions, the vacuum levels near the tip and sample surface are nearly in alignment to perform a noninvasive measurement. The dashed white circle in Fig. 3A outlines the region where the most dramatic changes occur during the quantum densification process when the local hole number increases from four to five as V_{bias} is increased as shown in Fig. 3, A to C. The red dots throughout Fig. 3 indicate the same locations of the holes in Fig. 3A so that changes in hole positions can be easily seen. The white arrow in Fig. 3B indicates the region where a new charge carrier arises as V_{bias} is raised from 1.9 to 2.0 V. A new

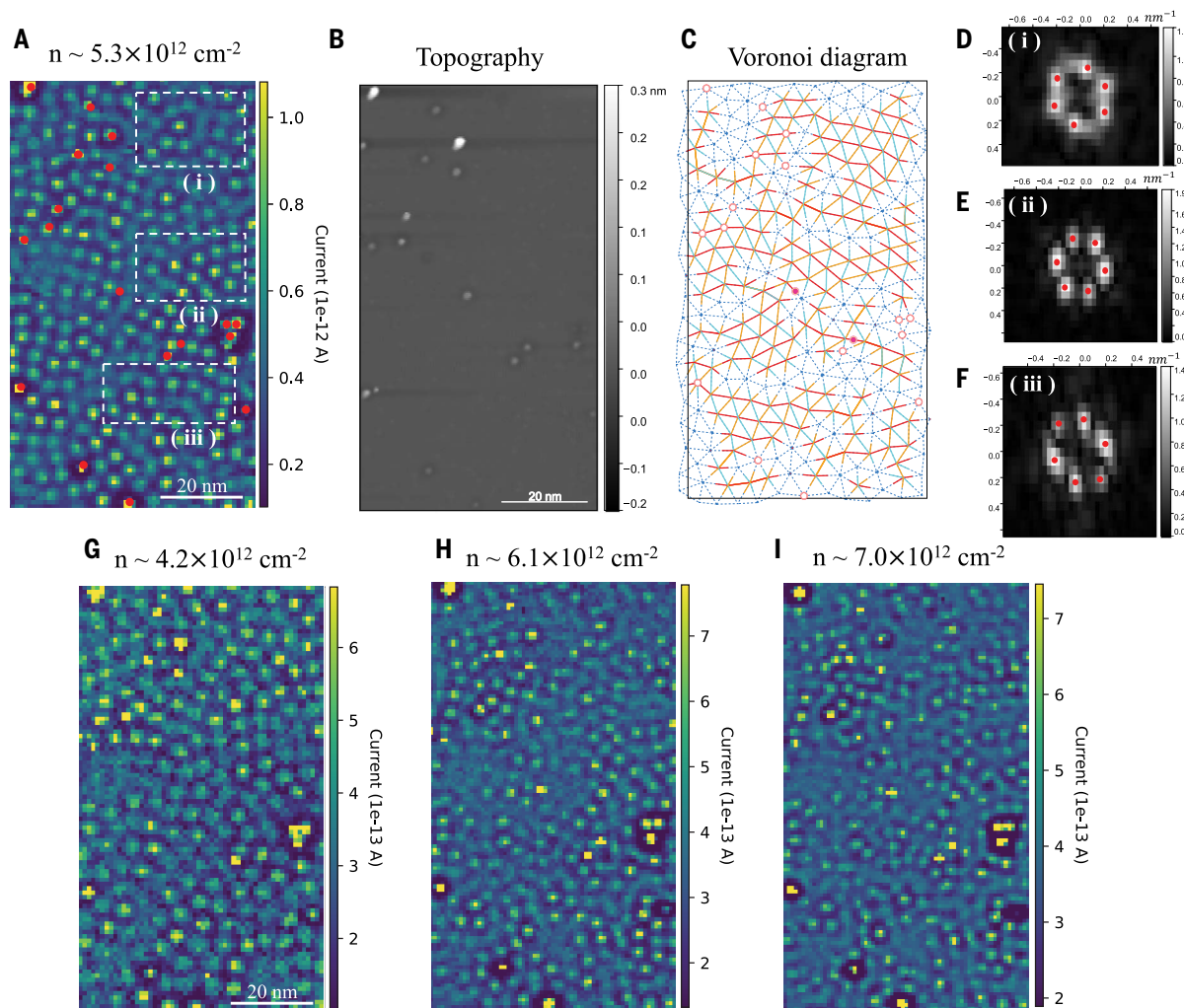


Fig. 2. Hole density dependence of a Wigner solid. (A) VBE tunnel current map of a Wigner solid in a 60- by 100-nm region of biMoSe₂ ($V_{\text{BG}} = -8 \text{ V}$, $V_{\text{bias}} = 1.9 \text{ V}$). The bright dots in the VBE tunnel current maps correspond to individual holes in the Wigner solid. Charged defects are indicated with red solid dots. (B) STM topographic image of the biMoSe₂ surface taken in the same region as (A) and (G) to (I). Most charged defects in the VBE maps correspond to defects in the topography image. (D to F) FFT images for regions (i), (ii), and (iii) showed in (A). A Nuttall window was used. The solid red dots indicate the peaks in the FFT images. (C) Crystal structure analysis of (A). Each intersection indicates a hole position calculated by applying a Voronoi cell partition method [(31), section 2]. Points connected with blue dashed lines indicate holes that have five or seven nearest neighbors, whereas points connected with colored solid lines indicate holes that have six nearest neighbors. The open red circles indicate charged defect positions as shown in (A). Solid red points indicate defects without a trapped hole. (G to I) VBE tunnel current maps of the same region shown in (A) for different hole densities controlled by using the bottom gate voltage V_{BG} . (G) $V_{\text{BG}} = -6 \text{ V}$, $V_{\text{bias}} = 2.2 \text{ V}$. (H) $V_{\text{BG}} = -10 \text{ V}$, $V_{\text{bias}} = 1.8 \text{ V}$. (I) $V_{\text{BG}} = -12 \text{ V}$, $V_{\text{bias}} = 1.5 \text{ V}$. $T = 5.4 \text{ K}$ for all the above measurements.

coalescence of charge is seen to gather at the location indicated in Fig. 3B with the white arrow, whereas the charge that was previously at the location of the red dot just above and to the right of the arrow is seen to slightly rise. All other holes remain close to the locations of the red dots. The process continued when the sample bias was raised to $V_{\text{bias}} = 2.1 \text{ V}$ (Fig. 3C). The new charge carrier was at that point fully incorporated in the Wigner solid. This process continued as shown in Fig. 3, C and D (V_{BG} decreasing to -8 V), in which the hole density further increased, causing a new coalescence of hole gathering around the location indicated in Fig. 3C with the white arrow. When $V_{\text{bias}} = 1.9 \text{ V}$, six holes exist in the center region (Fig. 3E) where previously (Fig. 3A) only four holes resided. The process continued as shown in Fig. 3, E and F, where an increase in V_{bias} caused a new coalescence of charge to appear at the region indicated with the arrow in Fig. 3F.

During the transition between integer-hole-number states under quantum densification, there is notable elongation or delocalization

of the hole wave functions. We observed similar behavior in other local regions during hole densification of the Wigner solid [additional data are provided in (31), section 7]. This behavior is a manifestation of the quantum mechanical nature of the hole lattice, in which quantum tunneling and delocalization of isolated holes can be substantial under suitable conditions even in the solid phase. By contrast, atom positions are almost always localized in disordered natural solids because of the much heavier mass of atoms.

Quantum melting

We next focused more strongly on the quantum melting behavior of the Wigner solid. This melting process is shown in Fig. 4 as the hole density ranges from $n = 5.3 \times 10^{12}$ to $7.0 \times 10^{12} \text{ cm}^{-2}$. At the highest hole density, we observed a mixed phase composed of solid regions with nanocrystalline domains and liquid regions with a smoother hole density distribution. We define liquid and solid regions as areas where

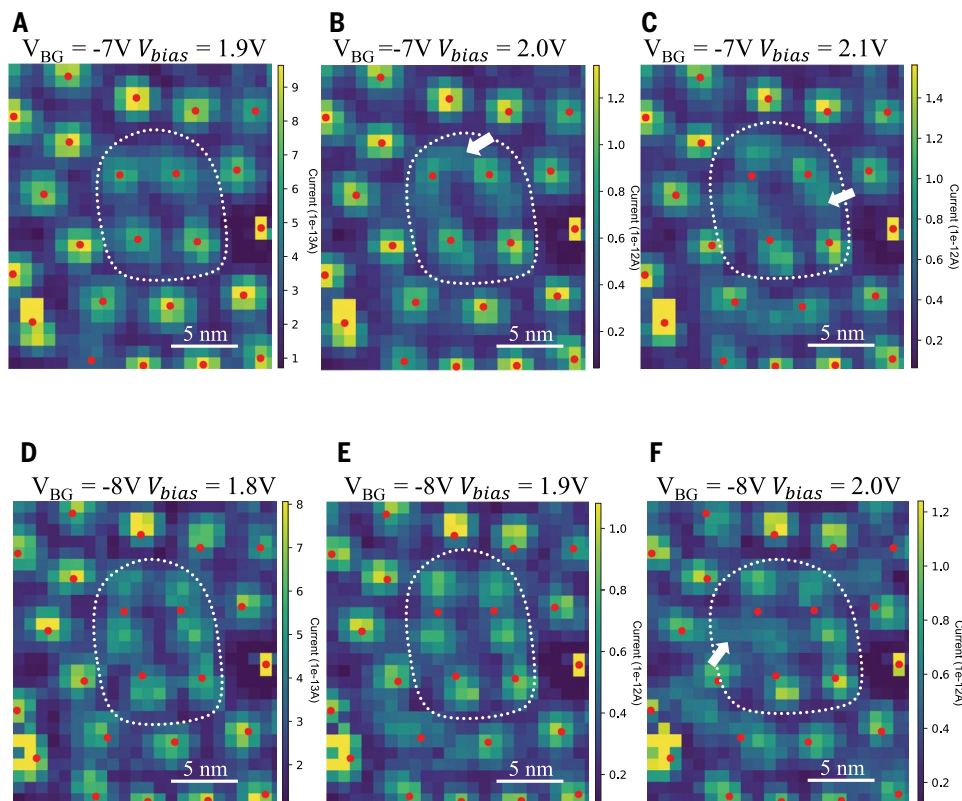


Fig. 3. Quantum densification of holes in a Wigner solid. VBE tunnel current maps show a Wigner solid with hole density increasing in fine steps by using both V_{BG} and V_{bias} (with negligible tip perturbation) [(31), section 1]. (A) $V_{BG} = -7V$, $V_{bias} = 1.9V$. (B) $V_{BG} = -7V$, $V_{bias} = 2.0V$. (C) $V_{BG} = -7V$, $V_{bias} = 2.1V$. (D) $V_{BG} = -8V$, $V_{bias} = 1.8V$. (E) $V_{BG} = -8V$, $V_{bias} = 1.9V$. (F) $V_{BG} = -8V$, $V_{bias} = 2.0V$. Solid red dots throughout indicate the initial location of holes shown in (A). The region indicated with a white dashed line in (A) to (F) shows (A) a local four-hole configuration, which evolves into (C) a well-resolved five-hole configuration and (E) six-hole configuration at higher densities. At the intermediate densities in (B) and (D), the wave function of local holes becomes partially delocalized (white arrows), a manifestation of the quantum nature of the Wigner hole solid. $T = 5.4$ K for all the above measurements.

the local tunnel current variation is lower and higher, respectively, than 28% over one Voronoi-cell size [(31) section 8]. The resulting boundaries between solid and liquid regions are indicated with two-toned solid lines in Fig. 4. The low-contrast liquid regions where holes are delocalized and have more widespread wave functions (close to the white boundary lines) can be clearly distinguished from the high-contrast solid regions where holes are more highly localized (close to the red boundary lines). The liquid-solid mixed phase extends over a rather broad hole density range of $5.7 \times 10^{12} < n < 7.0 \times 10^{12} \text{ cm}^{-2}$, which corresponds to the range of $19.7 < r_s < 21.8$ if we use a hole effective mass of $1.26m_e$ in biMoSe₂, based on the ab initio calculation [(31), section 3]. The value of r_s in this range is smaller than the theoretically predicted melting density of $r_s^* \approx 38$ for an ideal Wigner crystal (12, 14, 28). However, there is currently no experimentally measured hole effective mass for biMoSe₂. Previous studies have shown that measured effective masses for 2D TMDs can be much larger than theoretical predictions, creating a large uncertainty in our estimated r_s values (38).

Our melting data are qualitatively consistent with a percolation picture. For $n = 5.7 \times 10^{12} \text{ cm}^{-2}$, only small bubbles of the liquid phase are present (Fig. 4B), whereas at increased hole density, the liquid bubbles gradually expand (Fig. 4C). The bubbles are seen to eventually coalesce into an interconnected percolation network (Fig. 4D). Such percolation

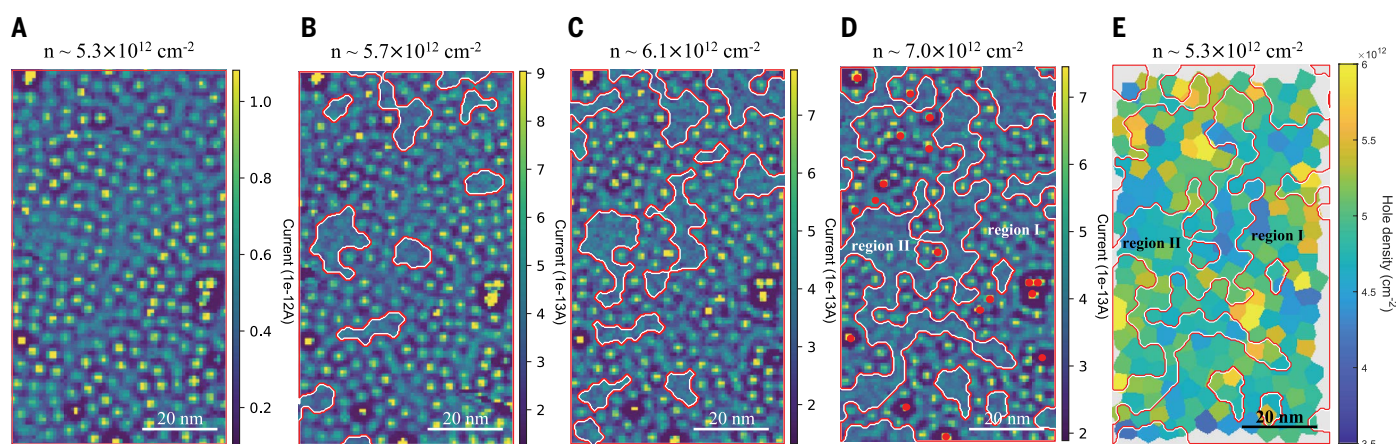


Fig. 4. Quantum melting of a Wigner solid. VBE tunnel current maps of a Wigner solid in biMoSe₂ show a gradual melting at high charge densities. (A) $V_{BG} = -8V$, $V_{bias} = 1.9V$. (B) $V_{BG} = -9V$, $V_{bias} = 1.8V$. (C) $V_{BG} = -10V$, $V_{bias} = 1.8V$. (D) $V_{BG} = -12V$, $V_{bias} = 1.5V$. The boundary between solid and liquid phase is distinguished by its local contrast difference and is outlined by two-colored solid lines. The red side indicates solid phase, whereas the white side indicates liquid phase. Wigner solid domains pinned by defects shrink with increasing charge density, whereas liquid regions expand and eventually induce percolative connectivity. We labeled the liquid phase and solid phase regions in (D) as region I and region II, respectively. The charged defects are indicated in (D) with solid red dots and are all localized in region I, suggesting that defect sites perform as pinning points. (E) The hole density distribution at $V_{BG} = -8V$, $V_{bias} = 1.9V$ (yellow is high, blue is low). The overlaid solid lines indicate region I and region II as defined in (D). The measured average charge densities in the two regions are identical within an experimental uncertainty of 2%. $T = 5.4$ K for all the above measurements.

behavior could potentially explain insulator-to-metal transitions seen for Wigner solids in previous transport studies (19, 20).

Discussion and outlook

Two very different theoretical mechanisms in the literature can potentially give rise to a solid-liquid mixture phase during the quantum melting of a 2D Wigner solid. In one mechanism, the disordered 2D material has long-range potential fluctuations that lead to spatially varying hole density regions within the sample. When the average hole concentration is close to the critical density of the Wigner solid, low-density regions will be in the solid phase ($r_s > r_s^*$), whereas the high-density regions will be in the liquid phase ($r_s < r_s^*$); solid and liquid regions are directly correlated with the long-range potential disorder. In the second mechanism, a solid and a liquid phase may coexist in an ideal 2DEG without defects. This spontaneous coexistence of solid and liquid phases during the quantum melting of a Wigner solid is called the “microemulsion” phase (39, 40). It is caused by a negative surface energy between the two different phases.

We can test the first mechanism by characterizing the long-range potential fluctuations in our system. If long-range potential fluctuations are the dominant effect, they should lead to persistent hole density fluctuation patterns at all gate voltages. To test this idea, we defined the liquid and solid regions in the mixed phase at $n = 7 \times 10^{12} \text{ cm}^{-2}$ ($V_{\text{BG}} = -12 \text{ V}$, $V_{\text{bias}} = 1.5 \text{ V}$) as regions I and II, respectively, and compared the average hole density in these two regions at lower gate voltages where the holes are in a solid phase everywhere. We used the inverse of the Voronoi cell area ($1/A_{\text{Voronoi}}$) to define the local hole density for low-density Wigner solid states at $n < 5.5 \times 10^{12} \text{ cm}^{-2}$ [details to determine solid and liquid boundaries are provided in (31), section 8]. In Fig. 4E, we show the hole density distribution based on the Voronoi cell analysis at $V_{\text{BG}} = -8 \text{ V}$, $V_{\text{bias}} = 1.9 \text{ V}$, which is overlaid with the boundaries of region I and region II. Substantial spatial variations are seen in the hole density at the unit cell level, but there are no pronounced long-range variations. The calculated average hole densities in region I and region II are identical within an experimental uncertainty of 2% [(31), section 10], and so no correlation exists between solid regions in the mixed phase and decreased local hole density, or between liquid regions in the mixed phase and increased local hole density. Therefore, the liquid-solid mixture phase in our system is not induced by a long-range potential fluctuation.

The second mechanism based on the microemulsion picture can generate a solid-liquid mixture phase in the absence of a long-range potential fluctuation. However, the microemulsion phase in an ideal 2DEG is expected to exist only in a very narrow phase region (41). This is in contradiction to the relatively wide phase coexistence density range ($\Delta n/n_c \geq 0.3$) observed in our experiment. Our data suggest that short-range disorders play a critical role in the Wigner crystal melting behavior, which is not included in the existing microemulsion theory.

We have visualized the quantum melting of a disordered Wigner solid, revealing the coexistence of solid and liquid phases during the melting process. The solid-liquid phase mixture observed in the presence of disorder cannot be fully captured by existing theories. Our observations provide insight into quantum melting behavior for Wigner crystals in 2D materials that exhibit defects.

REFERENCES AND NOTES

1. E. Wigner, *Phys. Rev.* **46**, 1002–1011 (1934).
2. R. S. Crandall, R. Williams, *Phys. Lett. A* **34**, 404–405 (1971).
3. Y. Cao *et al.*, *Nature* **556**, 80–84 (2018).
4. E. C. Regan *et al.*, *Nature* **579**, 359–363 (2020).
5. G. Chen *et al.*, *Nature* **579**, 56–61 (2020).
6. H. Li *et al.*, *Nature* **597**, 650–654 (2021).
7. J. Cai *et al.*, *Nature* **622**, 63–68 (2023).
8. J. Sung *et al.*, Observation of an electronic microemulsion phase emerging from a quantum crystal-to-liquid transition. arXiv:2311.18069 [cond-mat.str-el] (2023).

9. Y.-C. Tsui *et al.*, *Nature* **628**, 287–292 (2024).
10. A. A. Abrikosov, I. M. Khalatnikov, *Rep. Prog. Phys.* **22**, 329–367 (1959).
11. Yu. P. Monarkha, V. E. Syvokon, *Low Temp. Phys.* **38**, 1067–1095 (2012).
12. N. D. Drummond, R. J. Needs, *Phys. Rev. Lett.* **102**, 126402 (2009).
13. B. Spivak, S. V. Kravchenko, S. A. Kivelson, X. P. A. Gao, *Rev. Mod. Phys.* **82**, 1743–1766 (2010).
14. B. Tanatar, D. M. Ceperley, *Phys. Rev. B Condens. Matter* **39**, 5005–5016 (1989).
15. B. Spivak, S. A. Kivelson, *Ann. Phys.* **321**, 2071–2115 (2006).
16. C. Attaccalite, S. Moroni, P. Gori-Giorgi, G. B. Bachelet, *Phys. Rev. Lett.* **88**, 256601 (2002).
17. V. T. Dolgoplov, A. Gold, *JETP Lett.* **71**, 27–30 (2000).
18. G. Zala, B. N. Narozhny, I. L. Aleiner, *Phys. Rev. B Condens. Matter* **64**, 214204 (2001).
19. M. J. Manfra *et al.*, *Phys. Rev. Lett.* **99**, 236402 (2007).
20. S. Das Sarma *et al.*, *Phys. Rev. Lett.* **94**, 136401 (2005).
21. X. P. A. Gao *et al.*, *Phys. Rev. B Condens. Matter Mater. Phys.* **73**, 241315 (2006).
22. E. P. De Poortere, E. Tutuc, Y. P. Shkolnikov, K. Vakil, M. Shayegan, *Phys. Rev. B Condens. Matter* **66**, 161308 (2002).
23. M. S. Hossain *et al.*, *Phys. Rev. Lett.* **129**, 036601 (2022).
24. J. Falson *et al.*, *Nat. Mater.* **21**, 311–316 (2022).
25. V. J. Goldman, M. Santos, M. Shayegan, J. E. Cunningham, *Phys. Rev. Lett.* **65**, 2189–2192 (1990).
26. J. Yoon, C. C. Li, D. Shahar, D. C. Tsui, M. Shayegan, *Phys. Rev. Lett.* **82**, 1744–1747 (1999).
27. S. T. Chui, B. Tanatar, *Phys. Rev. Lett.* **74**, 458–461 (1995).
28. K.-S. Kim, C. Murthy, A. Pandey, S. A. Kivelson, *Phys. Rev. Lett.* **129**, 227202 (2022).
29. Y. Zhou *et al.*, *Nature* **595**, 48–52 (2021).
30. T. Smoleński *et al.*, *Nature* **595**, 53–57 (2021).
31. Supplementary text and data are available as supplementary materials.
32. H. Li *et al.*, *Science* **385**, 86–91 (2024).
33. S. Liu *et al.*, *ACS Nano* **17**, 16587–16596 (2023).
34. S. Barja *et al.*, *Nat. Commun.* **10**, 3382 (2019).
35. B. Schuler *et al.*, *Sci. Adv.* **6**, eabb5988 (2020).
36. C. A. Murray, P. L. Gammel, D. J. Bishop, D. B. Mitzi, A. Kapitulnik, *Phys. Rev. Lett.* **64**, 2312–2315 (1990).
37. P. Kim, Z. Yao, C. M. Lieber, *Phys. Rev. Lett.* **77**, 5118–5121 (1996).
38. Y. Zhang *et al.*, *Nat. Nanotechnol.* **9**, 111–115 (2014).
39. B. Spivak, *Phys. Rev. B Condens. Matter* **67**, 125205 (2003).
40. B. Spivak, S. A. Kivelson, *Phys. Rev. B Condens. Matter Mater. Phys.* **70**, 155114 (2004).
41. S. Joy, B. Skinner, *Phys. Rev. B* **108**, L241110 (2023).
42. Z. Xiang, Replication data for: Imaging quantum melting in a disordered 2D Wigner solid. Harvard Dataverse, V1 (2025); <https://doi.org/10.7910/DVN/CDWJEH>

ACKNOWLEDGMENTS

The authors acknowledge helpful discussion with S. Kivelson and P. Kim. **Funding:** This work was primarily funded by the US Department of Energy, Office of Science, Basic Energy Sciences, Materials Sciences and Engineering Division under contract DE-AC02-05-CH11231 within the van der Waals heterostructure program KCWF16 (device fabrication, STM spectroscopy, theoretical analysis, and computations). Support was also provided by the National Science Foundation award DMR-2221750 (surface preparation). This research used the Lawrence computational cluster provided by the Lawrence Berkeley National Laboratory (supported by the US Department of Energy, Office of Basic Energy Sciences under contract DE-AC02-05-CH11231). This research also used resources of National Energy Research Scientific Computing Center (NERSC), a US Department of Energy Office of Science User Facility located at Lawrence Berkeley National Laboratory, operated under contract DE-AC02-05CH11231. S.T. acknowledges primary support from US Department of Energy SC0020653 (materials synthesis), NSF CMMI1825594 (nuclear magnetic resonance and transmission electron microscopy studies on crystals), NSF DMR-1955889 (magnetic measurements on crystals), NSF ECCS2052527 (for bulk electrical tests), DMR 2111812, and CMMI 2129412 (for optical tests on bulk crystals). K.W. and T.T. acknowledge support from the JSPS KAKENHI (grants 21H05233 and 23H02052) and World Premier International Research Center Initiative (WPI), MEXT, Japan. **Author contributions:** M.F.C. and F.W. conceived the project. Z.X., J.X., H.L., J.N., S.L., and Y.J. fabricated the heterostructure device. Z.X. and S.C. fabricated the shadow mask. Z.X., H.L., and J.X. performed the STM/scanning tunneling spectroscopy measurement. M.H.N. and S.G.L. performed the DFT calculations of the bMoSe_2 effective mass. Z.X., H.L., J.X., Z.G., Z.H., M.F.C., and F.W. discussed the experimental design and analyzed the experimental data. R.S., R.B., and S.T. grew the MoSe_2 crystals. K.W. and T.T. grew the hBN single crystal. All authors discussed the results and wrote the manuscript. **Competing interests:** The authors declare that they have no competing interests. **Data and materials availability:** All data shown in the main text and supplementary materials are available in the Harvard Dataverse (42). **License information:** Copyright © 2025 the authors, some rights reserved; exclusive licensee American Association for the Advancement of Science. No claim to original US government works. <https://www.science.org/about/science-licenses-journal-article-reuse>

SUPPLEMENTARY MATERIALS

science.org/doi/10.1126/science.ado7136
Materials and Methods; Supplementary Text; Figs. S1 to S9; Table S1; References (43–49)

Submitted 17 February 2024; accepted 14 March 2025

10.1126/science.ado7136